metals

MDPI

Article

High-Throughput Printability Screening of AlMgSi Alloys for Powder Bed Fusion

Freddy Leijon [1,2,*] and Johan Moverare [2]

[1] Hydro Extruded Solutions AB, Innovation & Technology, 612 81 Finspång, Sweden
[2] Department of Management and Engineering (IEI), Linköping University, 581 83 Linköping, Sweden; johan.moverare@liu.se
* Correspondence: freddy.leijon@hydro.com

Abstract: The importance of both recycling and additive manufacturing (AM) is increasing; however, there has been a limited focus on the development of AM alloys that are compatible in terms of recyclability with the larger scrap loops of wrought 5xxx, 6xxx and cast 3xx aluminium alloys. In this work, the powder bed fusion (PBF) printability of AlMgSi alloys in the interval of 0–30 wt% Mg and 0–4 wt% Si is screened experimentally with a high-throughput method. This method produces PBF-mimicked material by PVD co-sputtering, followed by laser remelting. Strong evidence was found for AlMgSi alloys being printable within two different composition ranges: Si + Mg < 0.7 wt% or for Si + 2/3 Mg > 4 wt% when Mg < 3 wt% and Si > 3 wt%. Increasing the amount of Mg and Si influences the grain structure by introducing fine columnar grains at the melt pool boundary, although the melt pool interior was unaffected. Hardness in an as-built state increased with both Mg and Si, although Si had a neglectable effect at low levels of Mg. Both the evaporative loss of Mg and the amount of Mg in solid solution increased linearly with the amount of Mg.

Keywords: aluminium alloys; AlMgSi; printability; powder bed fusion; high-throughput; screening

Citation: Leijon, F.; Moverare, J. High-Throughput Printability Screening of AlMgSi Alloys for Powder Bed Fusion. *Metals* **2023**, *13*, 1114. https://doi.org/10.3390/met13061114

Academic Editor: Qingbo Jia

Received: 12 April 2023
Revised: 4 May 2023
Accepted: 7 June 2023
Published: 13 June 2023

1. Introduction

As the recyclability of metals increases in importance, new emerging alloys for additive manufacturing (AM) should be designed with recyclability in mind. In terms of volume, a major part of all aluminium produced is either alloyed with Mg or Si or a combination, specifically as the wrought alloys in the 5xxx and 6xxx series or as cast 3xx series alloys. Although the levels of Mg and Si vary between the different alloys, alloying with the same elements still hugely simplifies recyclability, as the alloying elements are the same. For instance, cast 3xx scarp and wrought 5xxx alloys, containing high levels of Si and Mg, respectively, can be used for alloying Si and Mg into 6xxx alloys, and 6xxx scrap can be alloyed with Si to be produce 3xx castings. This occurs without any deterioration in between the lifecycles, as no other elements will accumulate.

Apart from the main alloying elements, minor elements such as Fe, Mn, Cr, Cu, Zn, Ti and B, are typically also added. These are either unintentionally added as impurities or intentionally added to tailor the alloy. If the material is not diluted with virgin aluminium in between lifecycles, those elements will accumulate over time. Elevated levels of Fe, Mn and Cr decrease ductility [1], Cu and Zn decrease the corrosion resistance [2,3] and Mn, Fe, Cr, Ti and Zr decrease electrical and thermal conductivity [4,5]. Hence, a new aluminium AM alloy should preferably not contain elements except those previously mentioned; furthermore, the levels should be as low as possible to reduce the need for dilution with primary Al, as this will increase the need for the primary production of aluminium.

The current commercially available AlSi10Mg AM alloy is highly recyclable, as it does not have any minor alloying elements to promote grain refinement (GF). However, the strength is moderate, with $R_{p0.2}$ in the range of 300 MPa [6,7] and its use is therefore limited.

To reach a higher strength in the AlSiMg alloy system, the level of Mg is required to increase, as this will enable higher solid solution hardening and/or precipitation hardening. This, however, comes with the drawback of reduced printability (the alloys ability to solidify crack-free during printing). Printability is mainly controlled by alloy properties such as solidification shrinkage, solidification interval and melt permeability. Together, they dictated the magnitude of tensile stress on the liquid at the final part of solidification. An increase in the Mg level increases the solidification shrinkage, as eutectic phases with a greater shrinkage are formed during the end of the solidification. Increasing the level of Si on the other hand improves melt permeability, as the viscosity of the melt is lowered [8]. The requirement of high-melt permeability is lowered with decreasing grain size; therefore, Ti, Zr or Sc elemental GFs [9–12] or compound GFs such as TiB_2, TiC or TiN, are added [13–16].

However, it is also possible to achieve GF by increasing the total amount of alloying elements, due to the effect of growth restriction [17].

Nevertheless, traditional wrought alloys such as 6082 and 6061 [9] (0.6–1.2 wt% Mg and 0.7–1.3 wt% Si) are not printable. Printability for AlSiMg alloys has been achieved in some recent development [18,19], with the addition of ~1 wt% of Ti and/or Zr GFs. However, compared to wrought alloys, the Ti addition is in the order of 10 times higher, and with additions of Zr, a new incompatible element would be introduced into the scrap loop. By selecting the right composition within AlSiMg (4.4 wt% Mg, 3.1 wt% Si), Li et al. [20] demonstrated that a crack-free alloy without the addition of GF is possible. However, today, the composition space of printable AlSiMg alloys is poorly understood.

Therefore, in this study, seek to map out the printability of GF free AlSiMg alloys and find potential composition spaces.

2. Materials and Methods

The method developed in [21,22] was used with a target setup, to produce bi-directional and partly perpendicular composition gradients (see Figure 1a–c). This method provides a good setup for studying large compositional ranges with a high composition resolution. The target setup consisted of three parts placed on two magnetrons. On the left magnetron, a 1050 A alloy target was placed, and on the right, a two-part target consisting of pure Mg at the bottom and a 1050 A + AlSi12 compound target at the top. All targets/target parts were produced in-house from either a 10 mm 1050 A sheet provided by Hydro Aluminium AS (Si and Fe < 0.10 wt% and remaining elements < 0.01 wt%) or 99.9 wt% Mg ingot from REMAG Leichtmetall GmbH (Steyr, Austria). The 1050 A + AlSi12 compound target was produced by milling out a 7 mm deep and 20 mm wide slot at the racetrack position of the 1050 A sheet and by CMT MIG welding, filling this with AlSi12. The welding wire for this was bought from ESAB AB (city, country).

A 600 × 230 × 10 mm substrate was cut from the same 1050A sheet material as the targets, and positioned in relation to the targets as in previous works [8,9] (see Figure 1c). To improve film adhesion, the substates were etched in 2 mol NaOH solution at 60 °C, followed by rinsing with deionized water. The deposition was carried out in the CemeCon CC800 PVD system (Würselen, Germany) in a 435 mPa Ar atmosphere for 7 h, using a constant magnetron power of 5 kW, and while the voltage and current fluctuated, it was by 400 V ± 20 V and 12.5 A ± 2 A on average. The substrate temperature reached a steady-state temperature of ~150 °C. During the last 15 min of the deposition, the right magnetron was shutoff so that only the fully 1050 A target deposited. This was done to even out the film reflectivity and thus provide a uniform laser response over the whole substrate during the following remelting.

To mimic powder bed fusion (PBF), the PVD film was laser-melted in an Aconity MIDI laser (1075 nm) PBF machine (Herzogenrath, Germany). To enable laser melting and SEM handling, the substrate was first cut into 8 plates of size 110 × 110 mm (see Figure 2a). The melt pattern, order and the laser parameters (340 W, 1000 mm/s and 100 µm hatch spacing) were the same as in [22]. Those laser parameters were selected to match the estimated film

thickness of ~180 µm. Before laser melting, the plate was heated to 100 °C and during laser melting, the temperature increased and reached 145–150 °C.

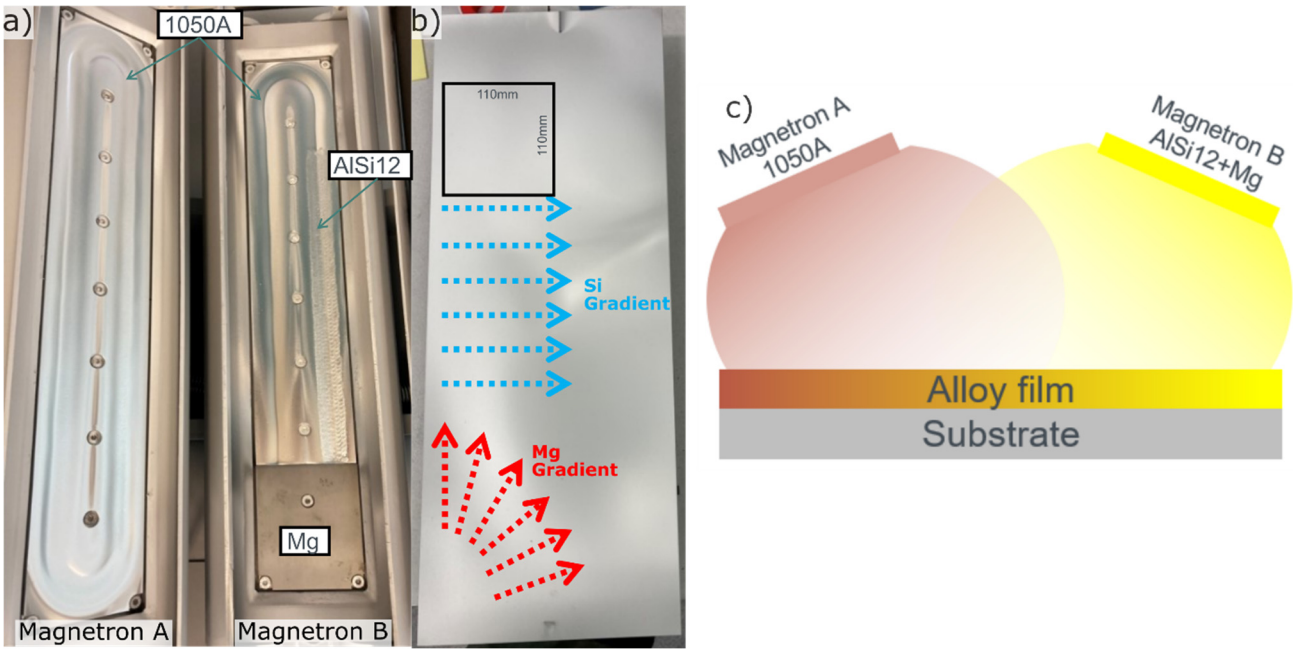

Figure 1. (**a**) Target setup. (**b**) Substrate with indication of Si and Mg gradient directions and one position of the cut plates for laser melting marked. (**c**) Cross-section of the target to the substrate setup.

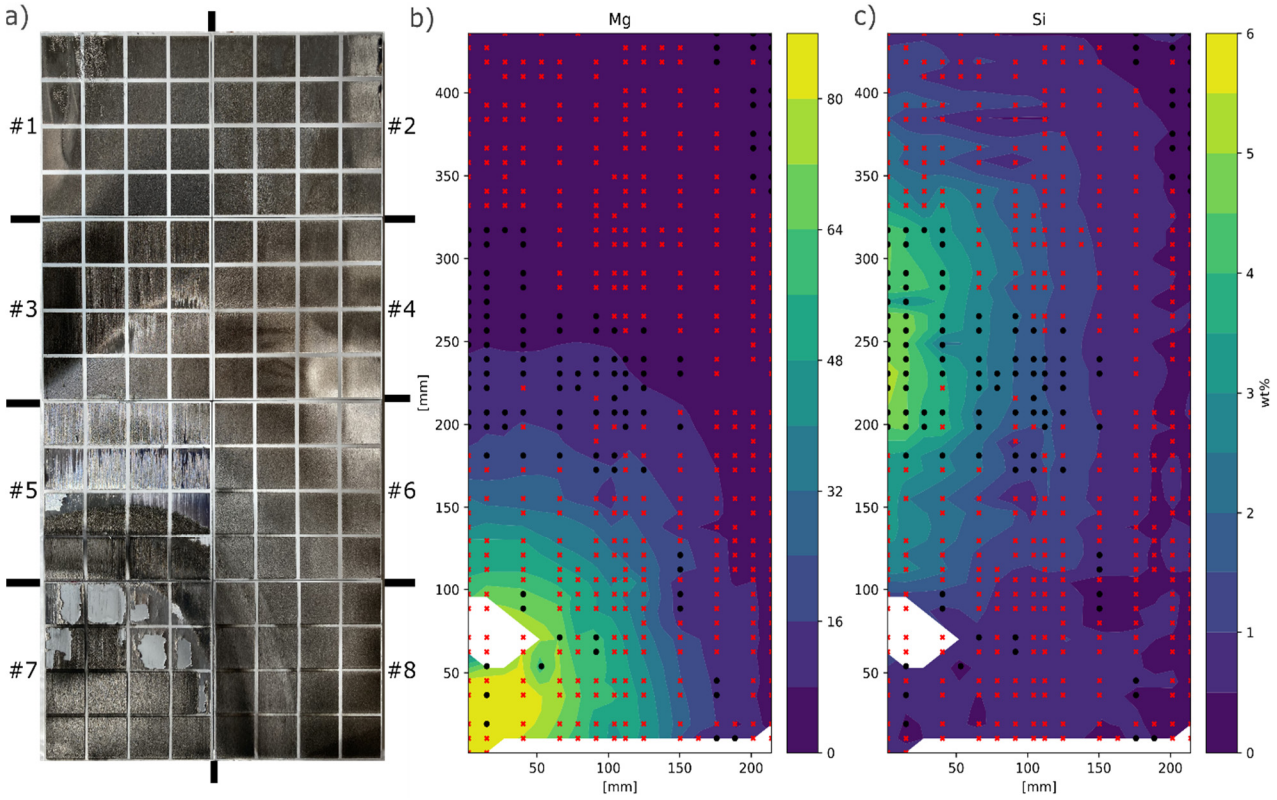

Figure 2. (**a**) Laser-melted plates, placed side by side as deposited with #1 top left and #8 bottom right. (**b**,**c**) Mg and Si composition mapped out and interpolated over the whole substrate. Black dot mark positions free from surface cracks and red cross positions with surface cracks. White areas indicated damaged/flaking film or faulty EDS measurements.

After laser melting, the composition was mapped out directly on the laser-melted surface of each sample plate, at 117 equally spaced position with EDS in FEI Nova nano-SEM 450 (Eindhoven, The Netherlands). To improve accuracy, each EDS measurement (at 15 kV) was carried out over a 4.5 mm^2 area for 35–45 s at each position. An image was also acquired in the SE mode of the measured position; this image was reviewed for surface cracks.

Microstructure investigations have been carried out on polished cross-sections in the SEM. The grain size was measured (Equivalent Circle Diamater) with EBSD (Oxford Instruments, High Wycombe, UK) on a 256 µm by 176 µm area, with a pixel size of 0.4 µm, located just beneath the top of the melted surface. An orientation difference of 10° was used for grain boundary identification. The grain statistics were calculated on all grain, except grain at the edge.

Hardness measurements were made with a DuraScan G5, with 50 g load, on the cross-sections perpendicular to the laser scan direction, with ~1 mm spacing between the indents and 100 µm spacing to the top surface. The measurements were made one year after the laser melting and no heat treatment was given before the measurement; thus, the material was in an "as-built" condition. To accurately map hardness against composition, 0.25–0.38 mm^2 area EDS measurements were also carried out along the cross-section, with a 2 mm spacing. The composition of the hardness indents was then linearly interpolated between the closest EDS measurement points. The hardness values were averaged over 0.5 wt% Mg × 0.5 wt% Si composition intervals, and only the intervals containing at least two measurements were used in the evaluation.

To investigate the amount of Mg in solid solution, XRD have been carried out. An 8 × 8 point grid evenly spaced over sample plate #6 was automatically scanned using a Bruker D8 Discovery diffractometer (Billerica, MA, USA) in a coupled 2theta mode. The position of the measurement was centred within each laser molten square, to minimize the potential signal from the un-molten PVD film. Mg in solid solution (SS) expands the lattice by 0.0044 Å/wt% Mg [8] (k_{Mg}) and thus shifts the Al peaks to lower angles. The lattice parameter can then be calculated through Bragg's law. As the (111) plane reflection at 38.6° has the highest intensity, a 34°–42° scan interval was selected. This interval also covered the peaks of the β-AlMg and Mg_2Si phases. From the k_{Mg} coefficient, Equation (1) could be used to calculate the amount of Mg in SS:

$$C_{MgSS} = \frac{(a_{measured} - a_{ref})}{k_{Mg}} \quad (1)$$

where $a_{measured}$ is the measured lattice parameter for the studied alloy and a_{ref} is the reference position. a_{ref} was calculated on the assumption of all Mg being in the SS at the position with the lowest Mg. At this position, Mg was only 0.85 wt%, and this amount of Mg could be trapped in SS, even using traditional methods such as extrusion. Using this position as C_{MgSS}, a_{ref} was calculated to be 4.035 Å.

3. Results and Discussion

The target setup resulted in a very large Mg gradient ranging from 0 to 85 wt% Mg, whereas Si only ranged from 0 to 6 wt% (see Figure 2c). From surface investigations, it could be concluded that Mg increased the surface roughness (see Figure 3. At Mg levels below 10 wt%, the periodicity of the laser pattern was visible, whereas above 10 wt%, the surface had a stochastic non-periodic appearance. The increase in surface roughness with the Mg content could be linked to the increased melt viscosity [8], a similar trend was also observed in the previous study [21]. Flaking of the film occurred in a region with ~75 wt% Mg, possibly caused by contamination or dry marks on the substrate prior to the deposition.

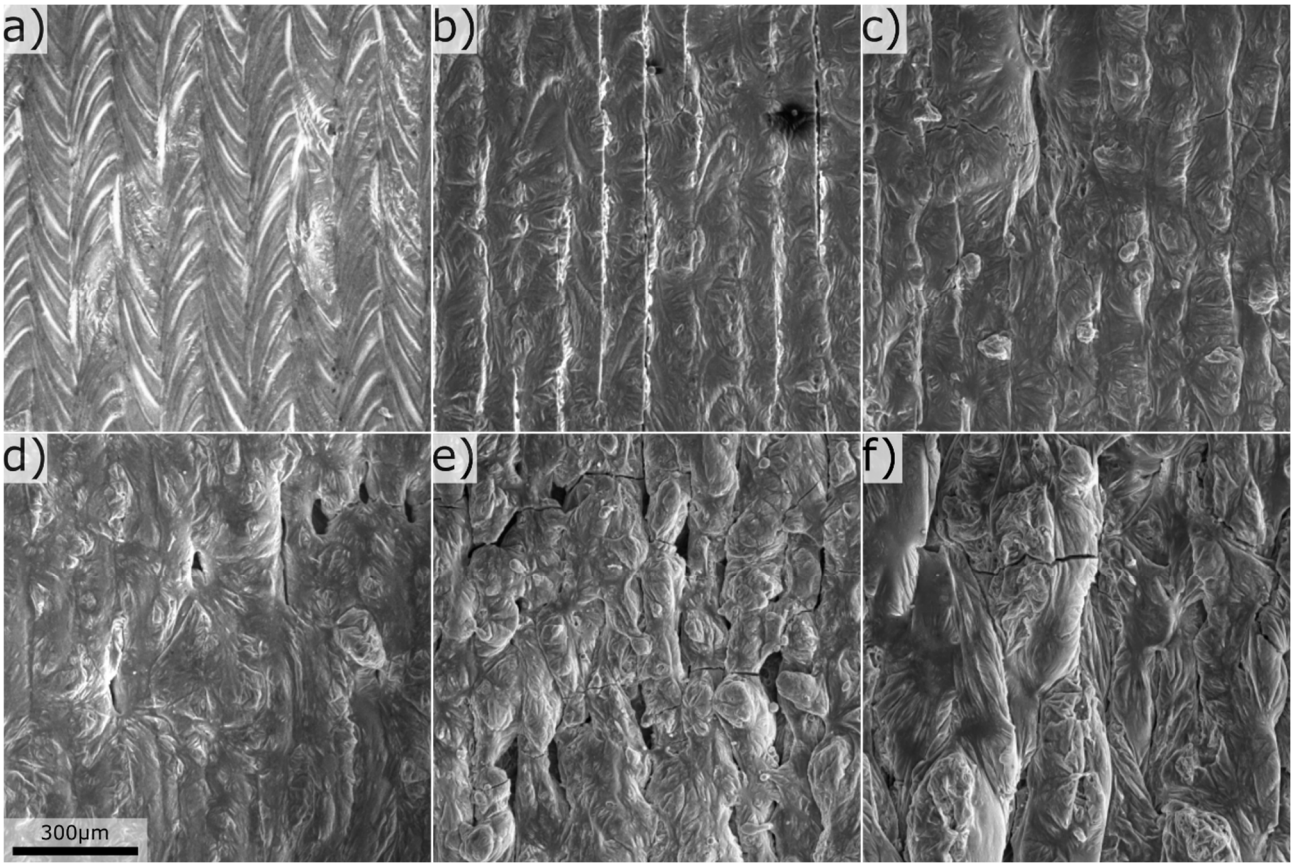

Figure 3. Laser-melted surface with a composition in wt% of (**a**) Mg 0.3, Si 0.4, (**b**) Mg 3.7, Si 0.8, (**c**) Mg 6.2, Si 0.5, (**d**) Mg 10.2, Si 3.4, (**e**) Mg 25.6, Si 0.6, (**f**) Mg 78.8, Si 0.7.

For most parts of the laser-melted surfaces, cracks were present; however, two crack-free areas were also present. By plotting the data in the Mg–Si space (see Figure 4), those areas were clearly revealed. The non-printable composition space could approximatively be demarcated by Si + Mg > 0.7 wt% and Si + 2/3 Mg < 4 wt%. This agreed well with data reported in the literature [9,20,23–27]. The lower printable space (Si + Mg > 0.7 wt%) was not as clear as the higher space, with a larger mix of observations. One contribution to the uncertainty is the higher relative measurement error in composition. For EDS at this composition level, the error is ±0.1 wt% for Si and Mg. Observation from cross-sections (see Figures 5 and 6) nearly confirmed the printability boarder observed from the surface cracks. However, the boarder at Mg > 3 wt% and Si < 3 wt% could not be confirmed due to the extensive degree of porosity observed. This porosity varied from very coarse (Figure 5c) to very fine (Figure 6b). Kimura et al. [24] also observed the increased porosity with additions of Mg, although they optimized the beam parameter for each composition. In the present work, only one set of beam parameters has been used; this set could have possibly been unsuitable for porosity formation at higher levels of Mg. Further studies should account for this by adjusting the beam parameters for Mg. Mg has a high vapor pressure and is one of few metals with substantial vapor pressure even in a solid state, this increasing the likelihood of porosity. Another possible source of porosity is the absorption of moisture in the columnar structure of the PVD film. The columnar structure varies both in distance to targets and composition, thus the amount of absorbed moister could vary with the position as well. However, as the plates were heated to 100 °C before remelting, it is expected that most of the moisture is evaporated. The time to reach 100 °C was approximately 20 min, followed by 10–20 min before the start of remelting.

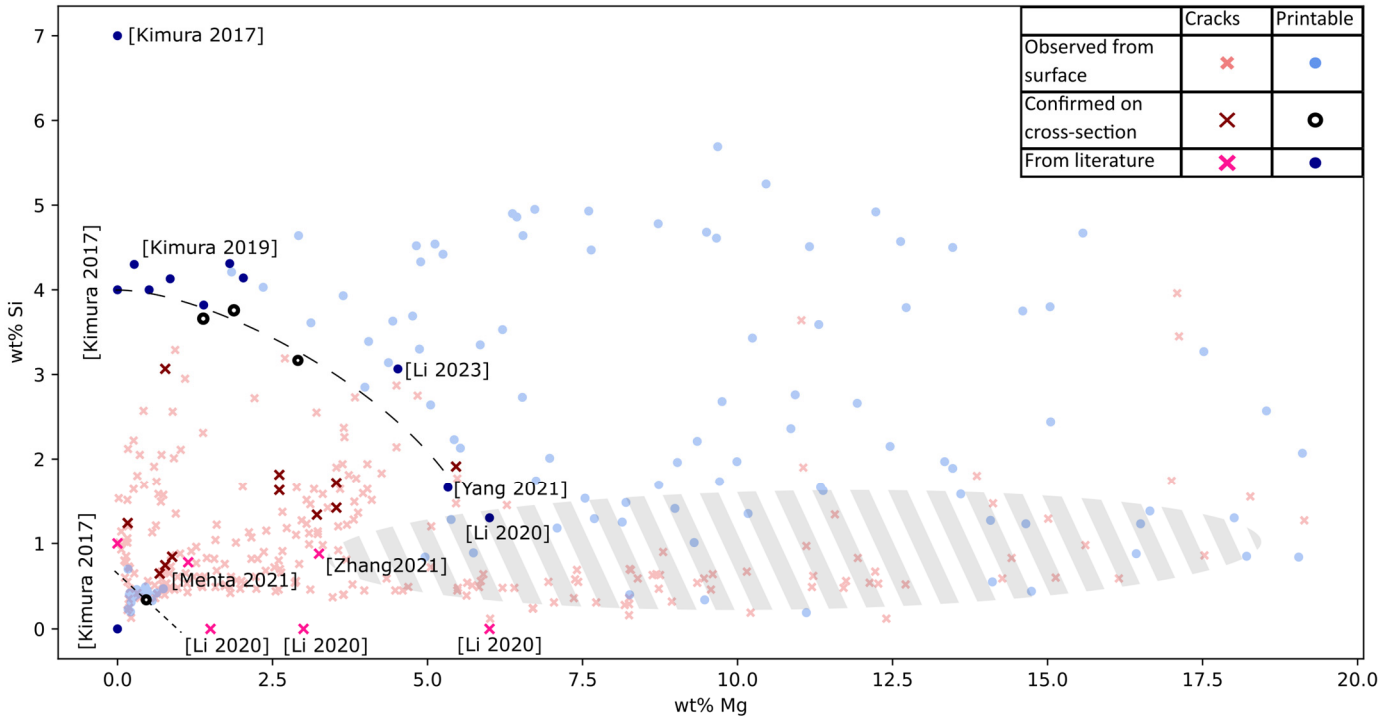

Figure 4. Printability mapped out in the Mg–Si composition space. Shaded area marks the area of high porosity [9,16,19,22,23,25,26].

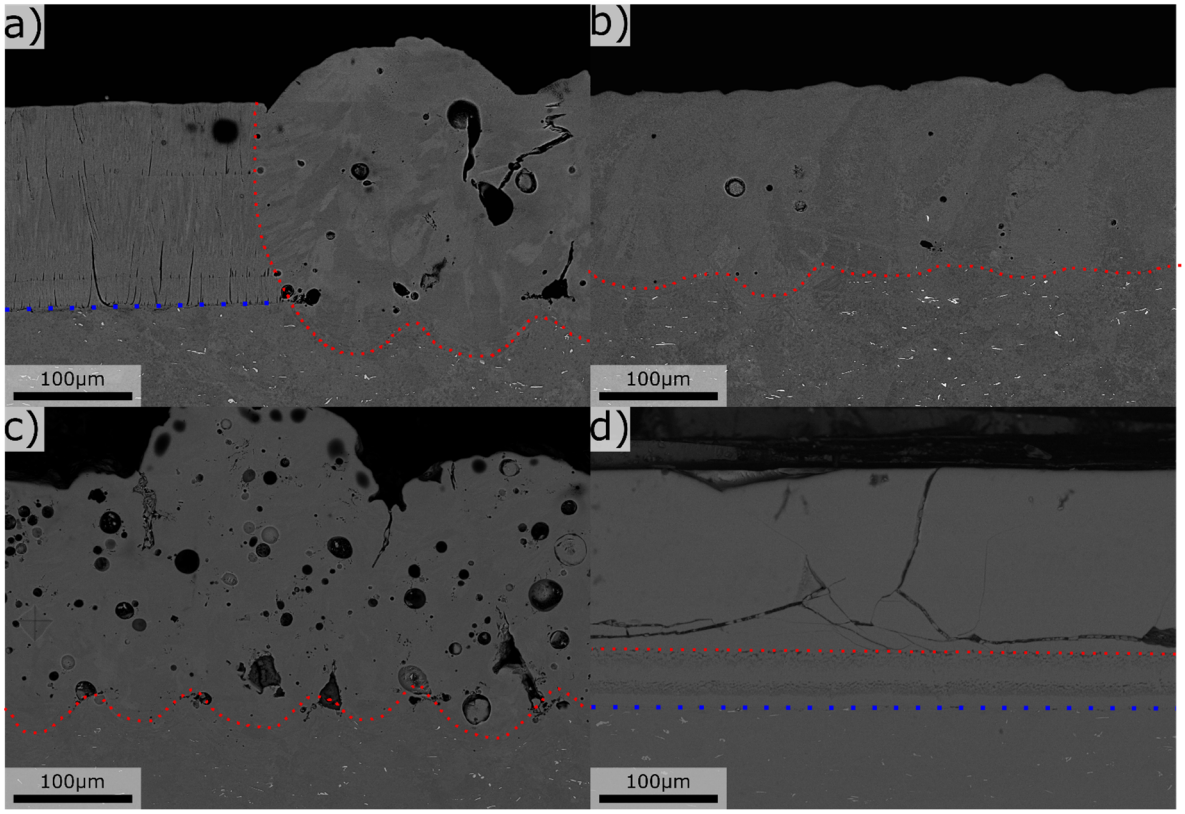

Figure 5. Cross-section overviews of laser melts: (**a**) Mg 2.4 Si 1.2, (**b**) Mg 0.2 Si 0.4, (**c**) Mg 7.8 Si 2.4, (**d**) Mg 34.5 Si 3.1. All units are in wt%. Dotted red line marks the border between the laser-melted (top) and non-melted areas (bottom), blue dotted line marks the border between the PVD film and substrate. White particles in the substrate are the AlFeSi phase, typically present in 1050 A.

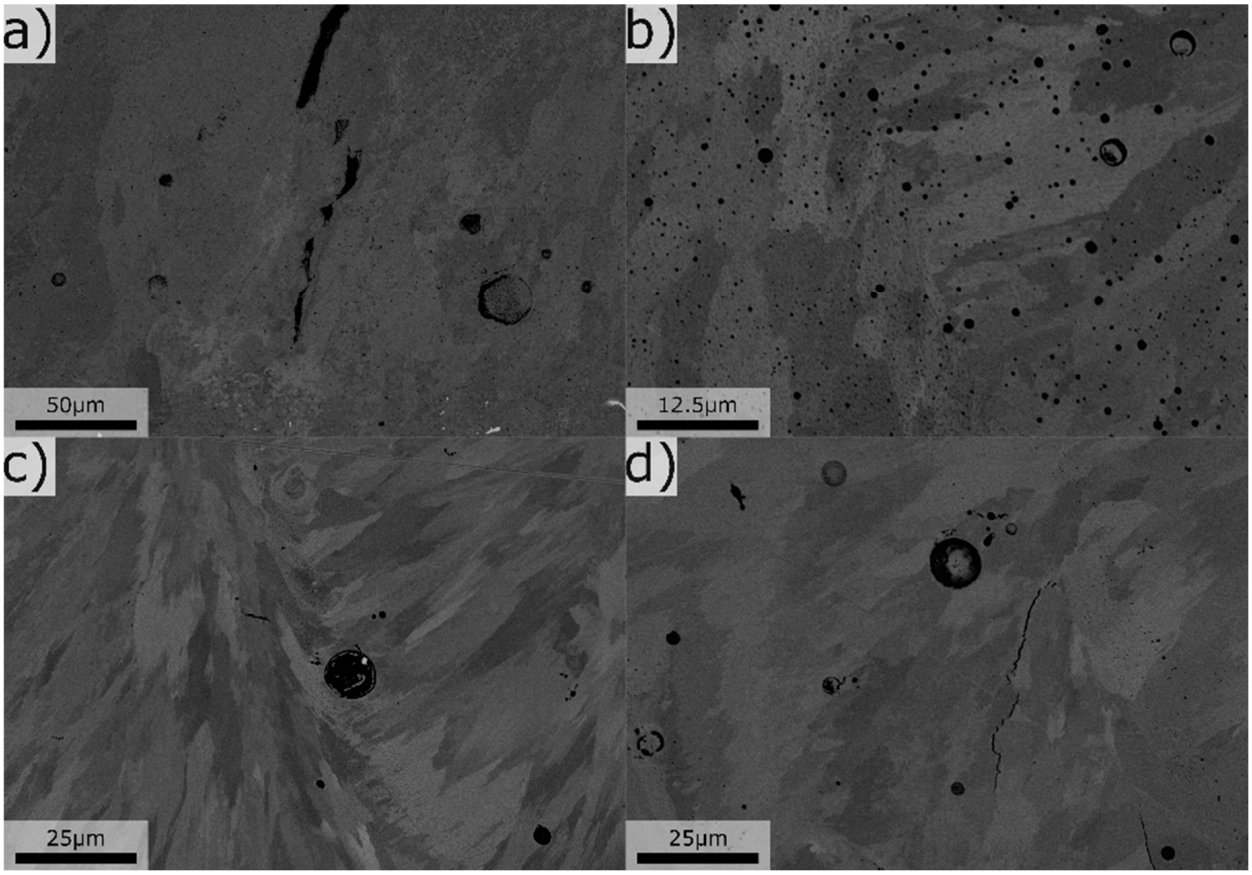

Figure 6. Typical microstructure for various compositions: (**a**) Mg 0.1 Si 1.4, (**b**) Mg 2.8 Si 3.2, (**c**) Mg 4.1 Si 2.4, (**d**) Mg 2.5 Si 1.8, all values are in wt%.

The high vapor pressure of Mg also leads to a loss of the element during laser melting. The loss of Mg was measured by comparing the composition of the unmolten PVD film with the laser-molten film in the close vicinity to each other (see Figure 7). The loss increased linearly with the Mg content, and the loss corresponds roughly to 10%, independent of composition. These results are close to the values reported by Kimura et al [24] using similar laser and scan parameters.

Interestingly, at Mg levels close to the stoichiometric β-AlMg phase (36 wt% Mg), no porosity was present, while cracks showed a brittle behaviour, indicating the formation of the β-AlMg phase. Since the PVD film had a columnar structure at this composition (see Figure 5d), the lack of porosity in the β-AlMg phase could be explained either by a lower solvability of H in the melt at the stoichiometric composition or a higher solvability in the solid β-AlMg phase.

The effect of Mg and Si on grain structure was most noticeable at the melt pool boundary, for which an increase had a refining effect (see Figure 8 and Table 1. This effect was visible from ~3 wt% Mg, suggesting that the Mg had a larger influence on grain size than Si, which is in line with the effect of the growth restricting factor [28] and also previous studies [24,26]. Although the melt pool boundaries had a layer of fine grains at ~8 wt% Mg, the melt pool interior still consisted of coarse grains.

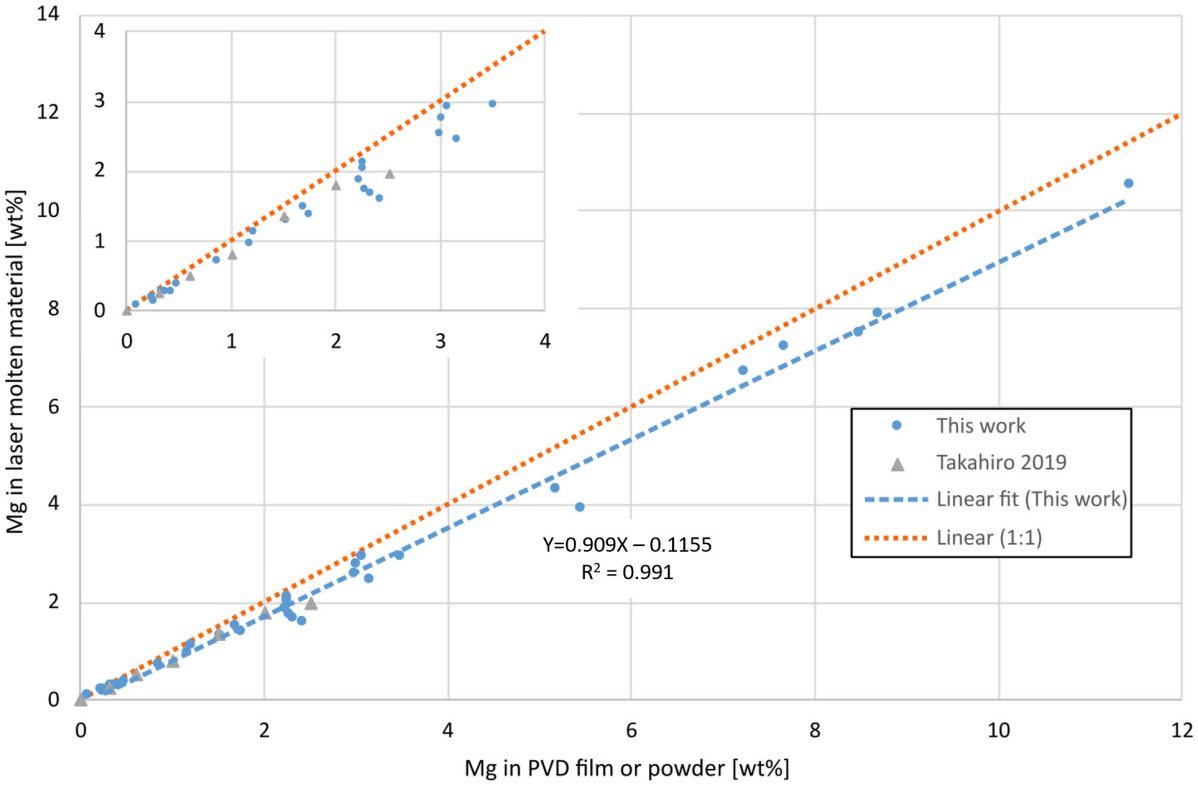

Figure 7. Mg content before (in PVD film) and after (laser molten), for different levels of Mg, [24].

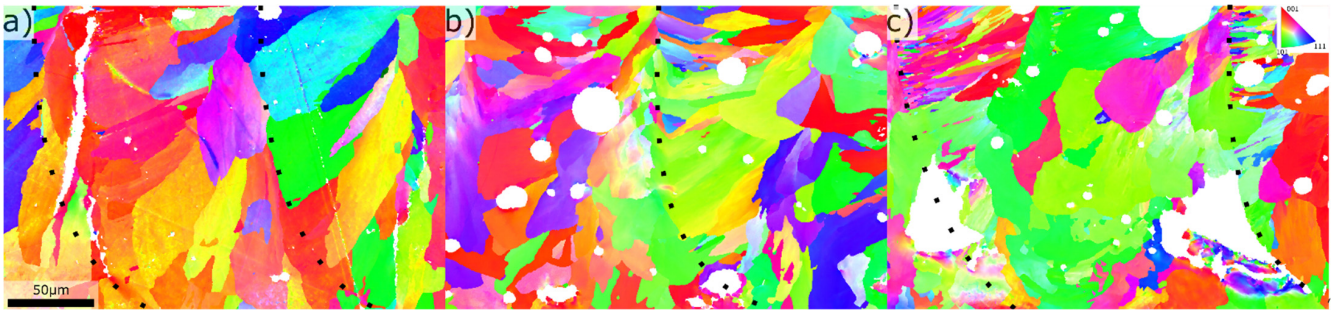

Figure 8. Grain structure for different alloy compositions: (**a**) 0.2 wt% Mg, 2.4 wt% Si, (**b**) 3.4 wt% Mg, 1.5 wt% Si; (**c**) 7.8 wt% Mg, 2.4 wt% Si. Dotted black line marks the melt pool boundary.

Table 1. Grain size at different Mg and Si contents. Std. is the standard deviation among the measured grains.

Mg [wt%]	Si [wt%]	Grain Size [µm]	Std. [µm]
0.2	0.5	13.0	15.2
0.2	2.4	10.4	13.6
3.4	1.5	10.7	12.2
7.8	2.4	5.9	8.9

Printability was further analysed by plotting the composition against the growth restricting factor (GRF) and the crack index (CI) $|\Delta T/(\Delta fs)^{\frac{1}{2}}|$, suggested in [29] (see Figure 9a), with GRF being defined by:

$$\text{GRF} = \sum c(K-1)m \quad (2)$$

where c is the concentration, K is the partitioning coefficient and m gradient of the liquidus for each element, assuming no interaction between the elements. The CI $|\Delta T/(\Delta fs)^{\frac{1}{2}}|$ was

calculated from Scheil solidification curves generated in ThermoCalc (TC-Python module) with TCAL8 database (see Figure 9b), where fs is the fraction solid and 0.87 < fs < 0.94 being used for calculating the CI. A low CI, given the same grain size, has the physical meaning of a longer time for liquid metal to refile the liquid to solid-phase change shrinkage, whereas a high CI is the opposite. This correlates well with solidification cracking, and thus has successfully been used for predicting printability. However, for high alloy contents, the last part of solidification consists of secondary-phase solidification at a constant temperature (see example composition IV and V in Figure 9b). In this case, the CI approaches zero and loses its physical meaning.

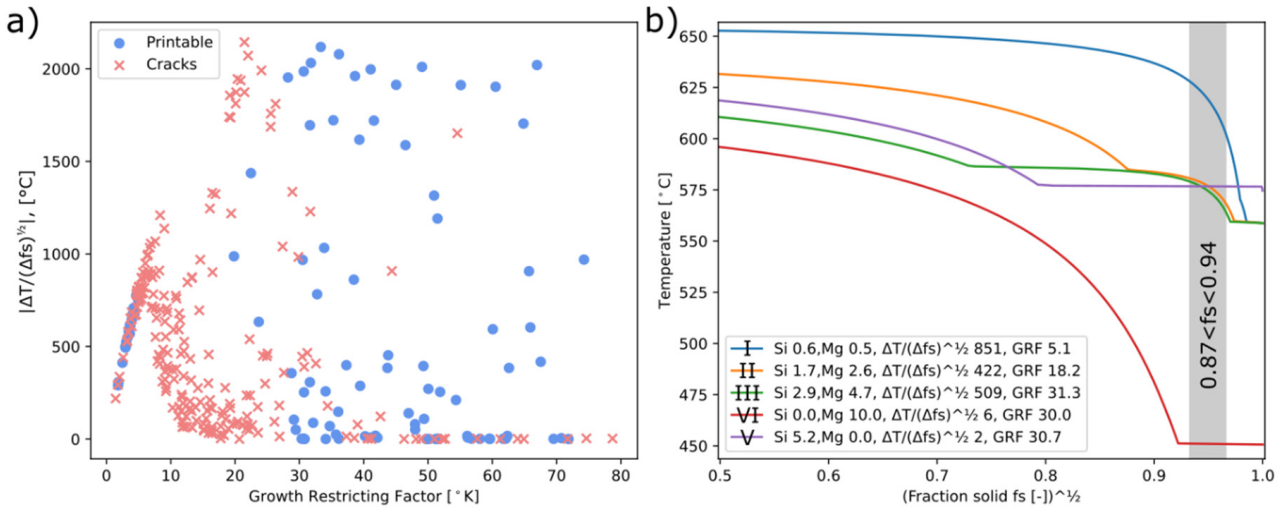

Figure 9. (**a**) Crack index $|\Delta T/(\Delta fs)^{\frac{1}{2}}|$ and growth restricting factor for compositions. Blue points mark the printable and red crosses the non-printable compositions. (**b**) Examples of Scheil solidification curves.

Looking at the Scheil curves, for a non-printable composition (example alloy II) and printable composition (example alloy III) in Figure 9b, the difference in shape in the critical solidification interval is small, and therefore so is the CI, whereas the GRF shows a larger increase. Despite some outliers, it is clear from Figure 9a that the GRF is a better predictor of printability than CI for CI > 10 and GRF > 10, which is in line with the small difference in the Scheil curve and CI for printable and non-printable compositions. However, for dilute alloys, there is no clear trend on printability with regards to either the CI or GRF.

Hardness in the as-built condition of the composition space Mg 0–12 wt% and Si 0–4 wt% is presented in Figure 10a. Hardness naturally varied strongly with the Mg content, while the effect of Si varied with the composition of Mg. In the Mg interval 0–2 wt%, a 2 wt% increase in Si had a negligible effect on the hardness, whereas at ~12 wt% Mg, the same increase in Si raised the hardness by 40–50 Hv, to reach a maximum of 240 Hv (see Figure 10b).

From the XRD spectrums, a clear shift of the Al FCC (111) peak towards lower angles could be observed, which corresponds to an increase in the lattice parameter *a* (see Figure 11a). Naturally, the β-AlMg and Mg2Si phase peak intensities also increase with Mg and Si, indicating the increasing amount of those phases. From the lattice parameter, the Mg in SS (Mg_{ss}) was estimated using Equation (1) (see Figure 11c). It was found that Mg_{ss} increased linearly with Mg. The accuracy in the lattice parameter was estimated to be ±0.0017 Å, leading to a Mg_{ss} error of ±0.39 wt%

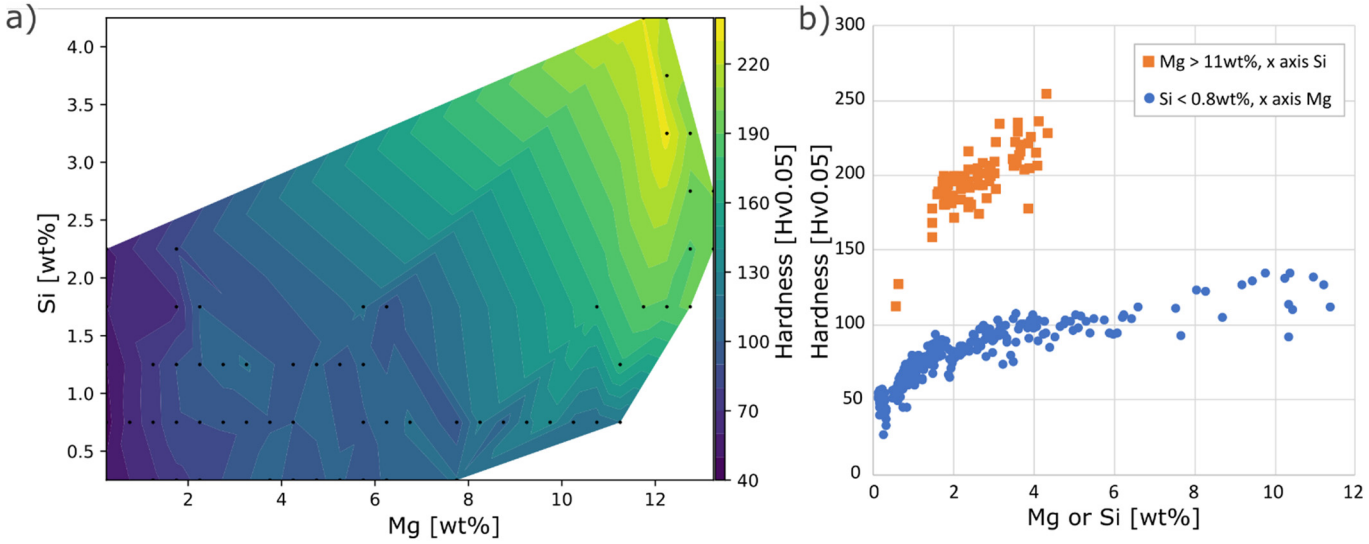

Figure 10. As-built hardness (**a**) mapped out in the Mg–Si composition space. Black dots mark the positions of average hardness in a 0.5 wt% composition interval. (**b**) The influence of Mg for Si < 0.8 wt% and Si for Mg > 11 wt%.

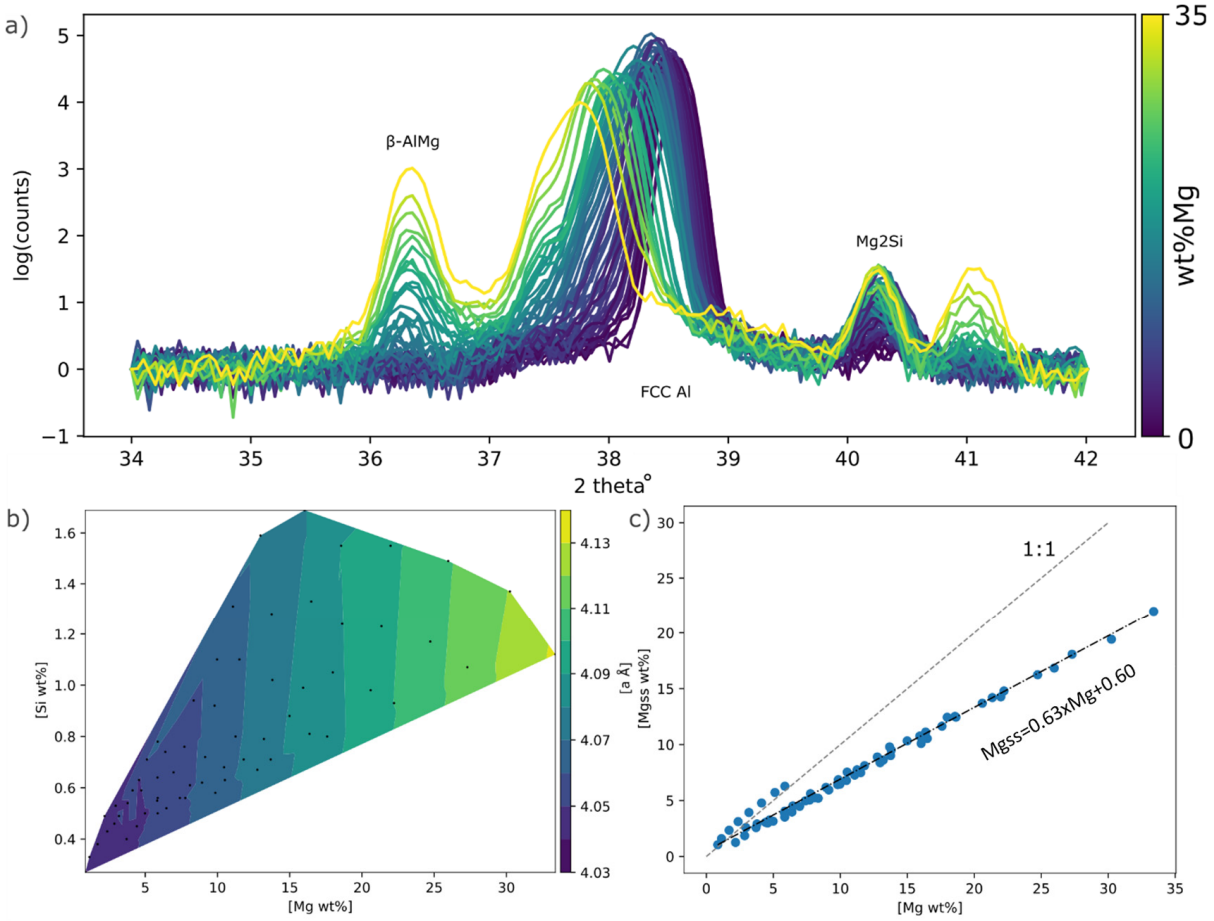

Figure 11. (**a**) XRD spectra for all points, (**b**) lattice parameter mapped out in Mg–Si composition space. Black dots indicate the XRD measurement position in the composition space. (**c**) Mg content against the estimated Mg in SS.

A classical description of SS hardening is:

$$\Delta\sigma = Hc^n \quad (3)$$

where c is the composition and the remaining parameters are constants. The exponent n for Mg in Al is close to unity when fitted for 0–3 wt% Mg [30], suggesting a linear increase in strength with Mg_{ss}. By calculating Mg_{ss} for the hardness data in Figure 10b (Si < 0.8 wt%), it was found that a linear fit poorly represents the relation between Mg_{ss} and hardness for the interval 0–12 wt%. The best fit was found for $Hv = 60 \times C_{Mgss}{}^{0.43}$. Comparing the same interval (0–3 wt% Mg) used in [30], n was 0.53, thus still far from unity. A possible explanation for the difference could be stress from second-phase precipitates also contributing to the peak shift, and thus the Mg_{ss} is falsely overestimated.

4. Conclusions

- Strong evidence was found for AlMgSi alloys being printable in two different composition ranges. Either for Si + Mg < 0.7 wt% or for Si + 2/3 Mg > 4 wt% when Mg > 3 wt% and Si > 3 wt%.
- Grain refinement at the melt pool boundary increased with the Mg content.
- At low levels of Mg, the effect of Si was neglectable on hardness, whereas at Mg levels of ~12 wt% a 2 wt%, the addition of Si increased the hardness by 40–50 Hv to reach values up to 240 Hv.
- Both the amount of Mg in solid solution and the loss of Mg due to evaporation increased linearly with the Mg content.
- Porosity increased with Mg.

Author Contributions: Conceptualization, F.L.; methodology, F.L.; formal analysis, F.L.; investigation, F.L.; data curation, F.L.; writing—original draft preparation, F.L.; writing—review and editing, F.L. and J.M.; supervision J.M.; project administration, J.M.; funding acquisition, F.L and J.M. All authors have read and agreed to the published version of the manuscript.

Funding: This research was funded by Norsk Hydro ASA, the Swedish Agency for Innovation Systems via SIP LIGHTer, (Vinnova grant 2020-04266) and Carl Trygger's Foundation for Scientific Research contracts CTS 15:219 and CTS 14:431.

Data Availability Statement: The data supporting the findings of this study are available from the corresponding author upon reasonable request.

Acknowledgments: For laser remelting, the authors acknowledge AMEXCI AB for a good collaboration and support. Svein Skjervold is also acknowledged for supervision.

Conflicts of Interest: The authors declare no conflict of interest.

References

1. Hwang, J.Y.; Doty, H.W.; Kaufman, M.J. The effects of Mn additions on the microstructure and mechanical properties of Al–Si–Cu casting alloys. *Mater. Sci. Eng. A* **2008**, *488*, 496–504. [CrossRef]
2. Chuvil, V.N.; Nokhrin, A.V.; Kopylov, V.I.; Gryaznov, M.Y.; Shotin, S.V.; Likhnitskii, C.V.; Kozlova, N.A.; Shadrina, Y.S.; Berendeev, N.N.; Melekhin, N.V.; et al. Investigation of mechanical properties and corrosion resistance of fine-grained aluminum alloys Al-Zn with reduced zinc content. *J. Alloy. Compd.* **2022**, *891*, 162110. [CrossRef]
3. Rajasekhar, K.; Babu, V.S.; Davidson, M.J.; Raghavendra, G. Influence of copper addition on corrosion properties and hardness of Al–Cu/Al two-layered-structure composites. *Proc. Inst. Mech. Eng. Part C J. Mech. Eng. Sci.* **2022**, *236*, 3146–3159. [CrossRef]
4. Kammer, C. (Ed.) *Aluminium Handbook 1*; Aluminium-Verlag Marketing & Kommunikation GmbH: Düsseldorf, Germany, 1999.
5. Xu, X.; Feng, Y.; Yang, P.; Zhang, B.; Wang, Y.; Wang, Q.; Fan, X.; Ding, H. The influence of trace elements on the microstructures and properties of the aluminum conductors. *Results Phys.* **2018**, *11*, 1058–1063. [CrossRef]
6. Schuch, M.; Hahn, T.; Bleckmann, M. The mechanical behavior and microstructure of additively manufactured AlSi10Mg for different material states and loading conditions. *Mater. Sci. Eng. A* **2021**, *813*, 141134. [CrossRef]
7. Mei, J.; Han, Y.; Zu, G.; Zhu, W.; Zhao, Y.; Chen, H.; Ran, X. Achieving Superior Strength and Ductility of AlSi10Mg Alloy Fabricated by Selective Laser Melting with Large Laser Power and High Scanning Speed. *Acta Metall. Sin. Engl. Lett.* **2022**, *35*, 1665–1672. [CrossRef]
8. Mondolfo, L.F. *Aluminum Alloys: Structure and Properties*; Butterworths: London, UK, 1976.

9. Mehta, A.; Zhou, L.; Huynh, T.; Park, S.; Hyer, H.; Song, S.; Bai, Y.; Imholte, D.D.; Woolstenhulme, N.E.; Wachs, D.M.; et al. Additive manufacturing and mechanical properties of the dense and crack free Zr-modified aluminum alloy 6061 fabricated by the laser-powder bed fusion. *Addit. Manuf.* **2021**, *41*, 101966. [CrossRef]
10. Martin, J.H.; Yahata, B.D.; Hundley, J.M.; Mayer, J.A.; Schaedler, T.A.; Pollock, T.M. 3D printing of high-strength aluminium alloys. *Nature* **2017**, *549*, 365–369. [CrossRef]
11. Tan, Q.; Zhang, J.; Sun, Q.; Fan, Z.; Li, G.; Yin, Y.; Liu, Y.; Zhang, M.-X. Inoculation treatment of an additively manufactured 2024 aluminium alloy with titanium nanoparticles. *Acta Mater.* **2020**, *196*, 1–16. [CrossRef]
12. Jia, Q.; Rometsch, P.; Cao, S.; Zhang, K.; Wu, X. Towards a high strength aluminium alloy development methodology for selective laser melting. *Mater. Des.* **2019**, *174*, 107775. [CrossRef]
13. Li, X.; Li, G.; Zhang, M.-X.; Zhu, Q. Novel approach to additively manufacture high-strength Al alloys by laser powder bed fusion through addition of hybrid grain refiners. *Addit. Manuf.* **2021**, *48*, 102400. [CrossRef]
14. Mair, P.; Kaserer, L.; Braun, J.; Weinberger, N.; Letofsky-Papst, I.; Leichtfried, G. Microstructure and mechanical properties of a TiB2-modified Al–Cu alloy processed by laser powder-bed fusion. *Mater. Sci. Eng. A* **2021**, *799*, 140209. [CrossRef]
15. Xinwei, L.; Shi, S.; Shuang, H.; Xiaogang, H.; Qiang, Z.; Hongxing, L.; Wenwu, L.; Yusheng, S.; Hui, D. Microstructure, solidification behavior and mechanical properties of Al-Si-Mg-Ti/TiC fabricated by selective laser melting. *Addit. Manuf.* **2020**, *34*, 101326. [CrossRef]
16. Li, X.P.; Ji, G.; Chen, Z.; Addad, A.; Wu, Y.; Wang, H.W.; Vleugels, J.; Humbeeck, J.V.; Kruth, J.P. Selective laser melting of nano-TiB2 decorated AlSi10Mg alloy with high fracture strength and ductility. *Acta Mater.* **2017**, *129*, 183–193. [CrossRef]
17. Easton, M.; StJohn, D. Grain refinement of aluminum alloys: Part II. Confirmation of, and a mechanism for, the solute paradigm. *Metall. Mater. Trans. A* **1999**, *30*, 1625–1633. [CrossRef]
18. Zhang, X.X.; Lutz, A.; Andrä, H.; Lahres, M.; Sittig, D.; Maawad, E.; Gan, W.M.; Knoop, D. An additively manufactured and direct-aged AlSi3.5Mg2.5 alloy with superior strength and ductility: Micromechanical mechanisms. *Int. J. Plast.* **2021**, *146*, 103083. [CrossRef]
19. Riener, K.; Nagler, A.; Letofsky-Papst, I.; Leichtfried, G. Processing of Aluminum Alloy 6182 with High Scanning Speed in LPBF by In-Situ Alloying with Zr and Ti Powder. *Alloys* **2022**, *1*, 277–287. [CrossRef]
20. Li, F.; Li, Z.; Tang, C.; Zhang, L.; Tan, Q.; Chen, C.; Zhang, M.; Zhou, K. Design high-strength Al–Mg–Si alloy fabricated by laser powder bed fusion: Cracking suppression and strengthening mechanism. *Mater. Sci. Eng. A* **2023**, *864*, 144591. [CrossRef]
21. Leijon, F.; Wachter, S.; Fu, Z.; Körner, C.; Skjervold, S.; Moverare, J. A novel rapid alloy development method towards powder bed additive manufacturing, demonstrated for binary Al-Ti, -Zr and -Nb alloys. *Mater. Des.* **2021**, *211*, 110129. [CrossRef]
22. Leijon, F.; Johansson, E.; Lu, J.; Aling, B.; Skjervold, S.; Moverare, J. Investigation of Ti1−x(Zr,Ta,V,W)xB2 and Al_3Ti_1−x(Zr,V)x grain refiners in additively manufactured Al-2 wt%Cu alloys by a high throughput method. *Mater. Des.* **2022**, *222*, 111093. [CrossRef]
23. Kimura, T.; Nakamoto, T.; Mizuno, M.; Araki, H. Effect of silicon content on densification, mechanical and thermal properties of Al-xSi binary alloys fabricated using selective laser melting. *Mater. Sci. Eng. A* **2017**, *682*, 593–602. [CrossRef]
24. Kimura, T.; Nakamoto, T.; Ozaki, T.; Sugita, K.; Mizuno, M.; Araki, H. Microstructural formation and characterization mechanisms of selective laser melted Al–Si–Mg alloys with increasing magnesium content. *Mater. Sci. Eng. A* **2019**, *754*, 786–798. [CrossRef]
25. Zhou, L.; Hyer, H.; Chang, J.; Mehta, A.; Huynh, T.; Yang, Y.; Sohn, Y. Microstructure, mechanical performance, and corrosion behavior of additively manufactured aluminum alloy 5083 with 0.7 and 1.0 wt% Zr addition. *Mater. Sci. Eng. A* **2021**, *823*, 141679. [CrossRef]
26. Li, R.; Wang, M.; Li, Z.; Cao, P.; Yuan, T.; Zhu, H. Developing a high-strength Al-Mg-Si-Sc-Zr alloy for selective laser melting: Crack-inhibiting and multiple strengthening mechanisms. *Acta Mater.* **2020**, *193*, 83–98. [CrossRef]
27. Yang, H.; Zhang, Y.; Wang, J.; Liu, Z.; Liu, C.; Ji, S. Additive manufacturing of a high strength Al-5Mg2Si-2Mg alloy: Microstructure and mechanical properties. *J. Mater. Sci. Technol.* **2021**, *91*, 215–223. [CrossRef]
28. Easton, M.; StJohn, D. Grain refinement of aluminum alloys: Part I. the nucleant and solute paradigms—A review of the literature. *Metall. Mater. Trans. A* **1999**, *30*, 1613–1623. [CrossRef]
29. Kou, S. A criterion for cracking during solidification. *Acta Mater.* **2015**, *88*, 366–374. [CrossRef]
30. Ryen, Ø.; Holmedal, B.; Nijs, O.; Nes, E.; Sjölander, E.; Ekström, H.-E. Strengthening mechanisms in solid solution aluminum alloys. *Metall. Mater. Trans. A* **2006**, *37*, 1999–2006. [CrossRef]